

## IRAS F21013–0739: a possible evolutionary successor of an ultraluminous infrared galaxy \*

Xian-Min Meng<sup>1,2</sup>, Hong Wu<sup>1</sup> and Chen Cao<sup>3</sup>

<sup>1</sup> National Astronomical Observatories, Chinese Academy of Sciences, Beijing 100012, China  
[mengxm@nao.cas.cn](mailto:mengxm@nao.cas.cn)

<sup>2</sup> Graduate University of Chinese Academy of Sciences, Beijing 100039, China

<sup>3</sup> Shandong University at Weihai, Weihai 264209, China

Received 2010 October 15; accepted 2010 November 8

**Abstract** We present a stellar population synthesis study of a type II luminous infrared galaxy, IRAS F21013–0739. Optical images show clear characteristics of a merger remnant. The  $H$ -band absolute magnitude is  $M_H = -25.1$ , which is  $\sim 2$  times as luminous as  $L^*$  galaxies. Stellar populations are obtained through the stellar synthesis code *STARLIGHT*. We find that it experienced a recent starburst (SB) phase  $\sim 100$  Myr ago. By reconstructing the ultraviolet-to-optical spectrum, and adopting Calzetti et al. and Leitherer et al.’s extinction curves, we estimate the past infrared (IR) luminosities of the host galaxy and find it may have experienced an ultraluminous infrared galaxy phase which lasted for about 100 Myr. Its  $i$ -band absolute magnitude is  $M_i = -22.463$ , and its spectral type shows type 2 active galactic nucleus (AGN) characteristics. The mass of the supermassive black-hole is estimated to be  $M_{\text{BH}} = 1.6 \times 10^7 M_{\odot}$  (lower-limit). The Eddington ratio  $L_{\text{bol}}/L_{\text{Edd}}$  is 0.15, which is typical of Palomar-Green (PG) quasars. Both the nuclear SB and AGN contribute to the present IR luminosity budget, and the SB contributes  $\sim 67\%$ . On the diagram of IR color versus IR/optical excess, it is located between IR quasars and PG quasars. These results indicate that IRAS F21013–0739 has probably evolved from a ULIRG, and it can possibly evolve into an AGN.

**Key words:** infrared: galaxies — galaxies: evolution — galaxies: starburst — galaxies: individual (IRAS F21013–0739) — galaxies: stellar content

### 1 INTRODUCTION

Ultraluminous infrared galaxies (ULIRGs;  $L_{\text{IR}} = L(8\text{--}1000 \mu\text{m}) > 10^{12} L_{\odot}$ ) are commonly regarded as galaxies with violent star-forming activity, which have great amounts of ultraviolet-to-optical radiation from their young, luminous stars attenuated by dust and re-emitted in the form of thermal dust emission in the infrared and submillimeter bands (Houck et al. 1984; Soifer et al. 1984). These galaxies always show signs of tidal interactions and mergers, which are responsible for triggering extreme nuclear activity and more widespread starburst (SB) activity (Toomre & Toomre 1972; Larson & Tinsley 1978). The interaction/merger rate increases with IR luminosity, and nearly all ULIRGs

---

\* Supported by the National Natural Science Foundation of China.

show signs of interaction/merger events (Sanders et al. 1988a; Melnick & Mirabel 1990; Zou et al. 1991; Murphy et al. 1996; Clements et al. 1996; Wu et al. 1998; Kim et al. 2002; Veilleux et al. 2002)

A large fraction of luminous infrared galaxy (LIRGs)/ULIRGs can be classified as Seyfert 1 or Seyfert 2 galaxies (Wu et al. 1998; Kewley et al. 2001). The fraction increases dramatically with IR luminosity, and among ULIRGs, the fraction reaches  $\sim 50\%$  (Kim et al. 1998a; Veilleux et al. 1999; Cao et al. 2006; Yuan et al. 2010), or even higher ( $\sim 70\%$ ; Nardini et al. 2010). Some of these types of objects are found to be dominated by an active galactic nucleus (AGN) in their bolometric luminosity (Boller et al. 2002; Nandra & Iwasawa 2007), but in most cases, these objects are SB dominated (Gu et al. 1997; Lutz et al. 1999; Franceschini et al. 2003); Nardini et al. (2008) proposed a fraction of  $\sim 85\%$ .

An evolutionary connection between ULIRGs and quasars was proposed by Sanders et al. (1988a, 1988b). They suggested that ULIRGs may represent the dust-enshrouded phase of quasars. A merger of gas-rich spirals causes gas to concentrate in the nucleus and trigger a nuclear SB, which is responsible for ULIRGs IR luminosity. Once the dust in the nuclear region is swept away by the nuclear radiation pressure and supernovae, optical quasars would appear. Though the scenario is supported by many studies (Canalizo & Stockton 2000, 2001; Zheng et al. 2002; Hao et al. 2005; Kawakatu et al. 2006; Cao et al. 2008; Veilleux et al. 2009; Hou et al. 2009), Genzel et al. (2001) and Tacconi et al. (2002) argue that ULIRGs as a class cannot evolve into optically bright quasars, because their dynamical parameters of the host galaxy and the mass of the central massive black-hole are different from optically bright quasars. Colina et al. (2001) proposed that high-luminosity quasars would be the end point in the merging process of massive ( $> L^*$ ) disk galaxies, which is supported by many studies (McLeod & Rieke 1994; Arribas & Colina 2003; Dasyra et al. 2006; Wolf & Sheinis 2008).

The unification model postulates that different types of Seyfert galaxies are essentially similar kinds of objects, and the observed differences between them are merely a matter of orientation-dependent obscuration (Antonucci 1993; Urry & Padovani 1995). In view of such a scheme, the evolutionary scenario of ULIRGs could also include type 2 IR galaxies. Another possible scenario is that type 2 bright IR galaxies may be obscured AGNs, which may be obscured by molecular clouds and dust from all viewing angles. When the obscuring materials have been driven away by the AGN, an unobscured, type 1 AGN would appear (Koulouridis et al. 2006). In any case, type 2 IR galaxies should contain vital clues to the evolutionary scenario problem. In this paper, we study this evolutionary problem through a type 2 LIRG: IRAS F21013–0739. Observations from IRAS, 2MASS, SDSS, HST and FIRST are presented in Section 2. The process of decomposing stellar populations and AGN spectra are in Section 3. Results of photometric and spectroscopic properties, star-forming and AGN activities, and past IR luminosities are shown in Section 4. Discussions and conclusions are given in Section 5. Throughout this paper, we adopt a cosmology with  $H_0 = 70 \text{ km s}^{-1} \text{ Mpc}^{-1}$ ,  $\Omega_M = 0.30$  and  $\Omega_\Lambda = 0.70$ .

## 2 OBSERVATIONS AND DATA REDUCTION

We adopt the multi-band data observed by the Sloan Digital Sky Survey (SDSS), recorded as SDSS J210358.74–072802.4, in both photometry and spectrometry, the Hubble Space Telescope (HST) Advanced Camera for Surveys (ACS) and the Wide Field Planetary Camera 2 (WFPC2), the Infrared Astronomical Satellite (IRAS), the Spitzer Space Telescope (Spitzer), the Two Micron All Sky Survey (2MASS) All-Sky Extended Source Survey and the Very Large Array (VLA) Faint Images of the Radio Sky at Twenty-centimeters (FIRST) survey.

The SDSS spectrum and images at  $u$ -,  $g$ -,  $r$ -,  $i$ -, and  $z$ -bands are taken from Data Release 5. They were observed with an exposure time of 53.9 s and the pixel size is  $0.396''$  on the sky. After Galactic reddening correction with  $E(B - V) = 0.015$  from dust maps by Schlegel et al. (1998) and

redshift correction with  $z = 0.137$  from SDSS calibration, the spectral coverage in the rest frame is 3355–8080 Å. An optical color map of  $g-r$  was made after coordinate system alignment, Galactic reddening correction,  $k$ -correction (IDL routine from Blanton et al. 2003, v4.1\_4), and smoothing by a Gaussian kernel with a radius of two pixels.

The HST WFPC2 archival image was observed with the filter F606W (the pivot characteristic wavelength was  $5996.8 \text{ \AA}$ )<sup>1</sup> and positioned on the Planetary Camera (PC) chip with a pixel scale of  $0.046'' \text{ pixel}^{-1}$ . The ACS image was observed by the Solar Blind Channel (SBC) with the filter F150LP (pivot wavelength  $1612.2 \text{ \AA}$ )<sup>2</sup>, and the pixel scale was  $\sim 0.032'' \text{ pixel}^{-1}$ .

The IRAS Faint Source Catalog (FSC) Version 2.0 is used to obtain the flux densities at 12, 25, 60 and  $100 \mu\text{m}$ . Only the  $60 \mu\text{m}$  flux density is high quality (FQUAL=3), which is  $0.3920 \text{ Jy}$ . The  $25 \mu\text{m}$  is moderate quality (FQUAL=2), and the other two are just upper limits (FQUAL=1). We do not make  $k$ -correction for IR fluxes, because the correction factor is small ( $\sim 5\%$  at  $60 \mu\text{m}$  for the M82 template) compared with the uncertainty of different  $k$ -correction methods and the uncertainty of IR luminosity calculations.

The Spitzer data include images from the Infrared Array Camera (IRAC) and Multiband Imaging Photometer for Spitzer (MIPS) observations and low resolution spectra from the Infrared Spectrograph (IRS). Basic Calibrated Data (BCD) of IRAC and MIPS were retrieved from the Spitzer public archive and were produced into single mosaic images at each band using the software MOPEX<sup>3</sup>. The mosaicked images of IRAC consist of four broad band images at  $3.6$ ,  $4.5$ ,  $5.8$ , and  $8.0 \mu\text{m}$  with a pixel size of  $0.6''$ , and pixel sizes of the MIPS images at  $24$ ,  $70$ , and  $160 \mu\text{m}$  are  $2.4''$ ,  $4''$  and  $8''$ , respectively. Our galaxy in IRAC  $3.6$  and  $4.5 \mu\text{m}$  images shows an extended structure, however, at longer wavelength bands, it is a point-source. Thus, extended- and point-source photometry and aperture correction are carried out depending on the given circumstance. The IRS mid-IR (MIR) spectra consist of observations of two low-resolution ( $R \sim 60 - 130$ ) modules (Short-Low [SL], Long-Low [LL]) from  $5.2$  to  $38 \mu\text{m}$  (see Houck et al. 2004 for a complete description). The spectra were reduced using SMART software (Higdon et al. 2004; Lebouteiller et al. 2010), including rogue pixel removal, sky subtraction, spectral extraction and analysis. The slit widths of SL and LL modules were  $\sim 3.6''$  and  $\sim 10.6''$ , and the  $5.8$ ,  $8.0$  and  $24 \mu\text{m}$  point-source full widths at half-maximum (FWHMs) were  $1.8''$ ,  $2.1''$  and  $6.2''$ , so the slits include almost all of the emission of the source. Therefore, aperture corrections for IRS spectra were not performed.

The  $1.4 \text{ GHz}$  continuum for the source was observed by FIRST. The integrated flux density in the archive is  $f_{1.4\text{GHz}} = 3.79 \text{ mJy}$ . The  $k$ -correction factor is calculated following Basu-Zych et al. (2007), which corrects the emission by  $(1+z)^\alpha$  with  $\alpha = 0.8$ , assuming the radio spectrum is in the form  $f_\nu \propto \nu^{-0.8}$ .

### 3 SPECTRAL SYNTHESIS

We derive stellar populations of the host galaxy from the SDSS spectrum, using the spectral synthesis code STARLIGHT (Cid Fernandes et al. 2005), which is a robust program that fits diverse objects from early type galaxies to spirals, AGNs, and so on. STARLIGHT fits the observed spectrum  $O_\lambda$  with a set of pre-defined template spectra, and searches for the minimum  $\chi^2$  value ( $\chi^2 = \sum_\lambda [(O_\lambda - M_\lambda)w_\lambda]^{-2}$ , where  $M_\lambda$  is the model spectrum,  $w_\lambda^{-1}$  is the error of  $O_\lambda$  at each wavelength) by means of a simulated annealing plus Metropolis scheme. The model spectrum  $M_\lambda$  is a linear combination of the pre-defined template spectra, which become extinct by  $A_V$  and are broadened by a Gaussian kernel centered at velocity  $v_\star$  and with velocity dispersion  $\sigma_\star$ .

<sup>1</sup> McMaster, M., Biretta, J., et al. 2008, WFPC2 Instrument Handbook, Version 10.0 (Baltimore: STScI) ([http://www.stsci.edu/hst/wfpc2/documents/IHB\\_17.html](http://www.stsci.edu/hst/wfpc2/documents/IHB_17.html)).

<sup>2</sup> Maybhate, A., et al. 2010, "ACS Instrument Handbook", Version 10.0 (Baltimore: STScI) (<http://www.stsci.edu/hst/acs/documents/handbooks/cycle19/cover.html>).

<sup>3</sup> MOPEX web site: <http://ssc.spitzer.caltech.edu/dataanalysis/tools/mopex/>

### 3.1 Test Fitting and Parameter Determination

IRAS F21013–0739 is recorded as a quasar with  $M_i = -22.463$  in Schneider et al.'s (2007) fourth edition of the SDSS Quasar Catalog, but is rejected from the fifth edition of the catalog (Schneider et al. 2010). Its SDSS spectrum does not show a quasar-like featureless continuum (FC), and it is not clear whether it contains such a spectral component. Cid Fernandes et al. (2004) added an FC component of  $F_\nu \propto \nu^{-1.5}$  to the stellar base to represent the scattered FC in Seyfert 2s. Following Meng et al. (2010, hereafter M10), we carried out test fittings involving a power-law FC with  $F_\lambda \propto \lambda^{\alpha_\lambda}$  to verify whether it exists and found the value of the spectral index  $\alpha_\lambda$ . We let the spectral index vary from  $-3.0$  to  $-0.5$  at intervals of  $0.5$ , and  $\alpha_\lambda = 0$  for non-power-law cases.

Single metallicity SSPs from Bruzual & Charlot's stellar population evolution model (2003; hereafter BC03), whose ages are 0.005, 0.025, 0.1, 0.29, 0.5, 0.9, 1.4, 2.5, 4, and 10 Gyr, are adopted in each fitting. The best-fit metallicity and the AGN's power-law index are determined simultaneously, if they could give a minimum  $\chi^2$  value among all possible parameter combinations. The six metallicities in the test are  $Z = 0.0001, 0.0004, 0.004, 0.008, 0.02,$  and  $0.05$ . Following M10, we also carry out multiple fittings with 25 different seeds and adopt the mean value over all seeds for every parameter to obtain the most reliable parameter values.

Figure 1 gives the result of the test fitting. The minimum  $\chi^2$  appears at  $Z=0.008$  and  $\alpha_\lambda = -2.5$ . These values are reasonable for SB galaxies and AGNs, respectively (Francis 1996; Vanden Berk et al. 2001; Tadhunter et al., 2005; Pellerin & Robert 2007; Letawe et al. 2007), so we adopt these values for the formal fitting.

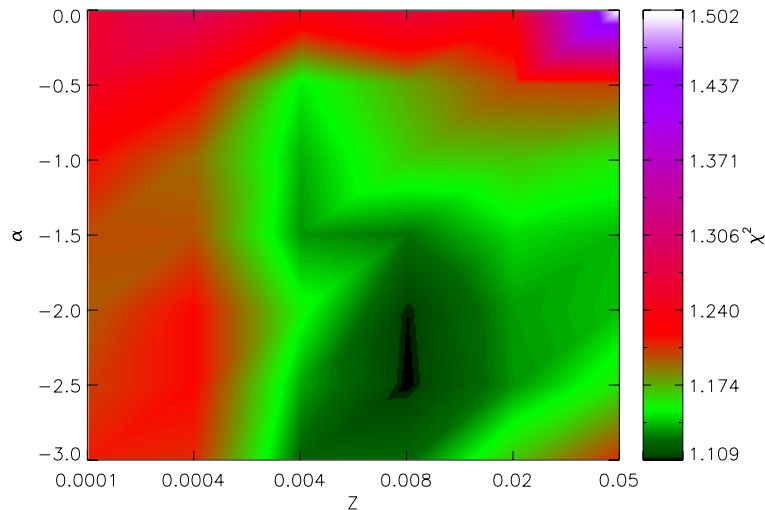


**Fig. 1** Power-law index and metallicity test. Each test fitting adopts one of the six metallicities, a certain power-law index and 10 SSPs, and is evaluated by averaged  $\chi^2$  values over 25 individual fittings with different seeds. The *left* panel shows the averaged  $\chi^2$  values versus metallicities ( $Z$ ) and power-law indices ( $\alpha$ ). The *right* panel gives the color code of  $\chi^2$ .

### 3.2 Formal Fitting and Stellar Populations

The formal fitting involves 50 independent fittings with different seeds. Stellar absorption lines are given a five times larger weight than the continuum to emphasize the detail of the stellar com-

ponent. Emission lines [O II]  $\lambda\lambda 3726+3729$  ([O II]  $\lambda 3727$ ), Ne III  $\lambda 3869$ , [O III]  $\lambda\lambda 4959+5007$ , [N I]  $\lambda\lambda 5198+5200$ , He I  $\lambda 5876$ , [O I]  $\lambda 6300$ , [N II]  $\lambda\lambda 6548+6583$ , and H I Balmer lines, together with the Na I D 5890 galactic interstellar medium absorption line are all masked and excluded from the fitting. The observed spectrum  $O_\lambda$  and all SSP templates are normalized at wavelength  $\lambda_0 = 4020 \text{ \AA}$  before fitting.

The formal fitting results are summarized and plotted in Figure 2. The top-left panel shows the observed SDSS spectrum  $O_\lambda$  (green), the model synthetic spectrum  $M_\lambda$  (red) and its stellar component (beige) and power-law component (black); the (blue) spectrum is the error of  $O_\lambda$ , and the inverse of error is the weight at each wavelength in the spectral fitting; the gaps in the error spectrum mark the masked emission line regions and the thrice weighted absorption lines; the bottom-left panel gives the residual spectrum  $E_\lambda = O_\lambda - M_\lambda$ ; the top-right panel shows the light-weighted stellar population fractions  $x_j$  (the left black bar represents the power-law FC fraction with an arbitrary age); the bottom-right panel shows the mass-weighted population fractions  $\mu_j$ .

Figure 2 indicates that the stellar populations of the galaxy consist of two main parts: an SB population whose age is  $\leq 100$  Myr (whose 290 Myr population is negligible) and a background population whose age is  $\geq 900$  Myr. The logarithmic mean age  $\langle \log t_\star \rangle_L$  that is weighted by light (Cid Fernandes et al. 2005), and the ones weighted by stellar mass,  $\langle \log t_\star \rangle_M$ , are 7.9 and 9.2, respectively. These figures indicate that the young populations dominate in light, and the old ones dominate in mass. The mean velocity dispersion is  $\sigma_\star = 317 \text{ km s}^{-1}$ , which is typical of giant ellipticals.

## 4 RESULTS

### 4.1 Photometric Properties

The SDSS  $u$ -,  $g$ -,  $r$ -,  $i$ -, and  $z$ -band magnitudes are listed in Table 1, where *fiberMag* is the magnitude measured within the  $3''$  fiber aperture, and *petroMag* is measured within the Petrosian radius.

**Table 1** Magnitudes from SDSS Fiber and Petrosian Photometry

mag	$u$	$g$	$r$	$i$	$z$
fiberMag	18.46	17.86	17.37	17.06	16.84
petroMag	17.90	17.00	16.34	16.02	15.82
k-correction	0.028	0.166	0.109	0.0213	0.086

Figure 3 (a) and (b) shows the HST WFPC2 F606W and the ACS SBC F150LP filter images. The high resolution image of WFPC2 clearly shows two luminous spots in the central region, whose spatial separation is  $\sim 1.6''$ . They must be two nuclei merging with each other in the galaxy’s merger phase. The brighter nucleus at the center is fully covered by the SDSS fiber aperture, and the fainter one is marginally covered by the fiber. The  $r$ -band flux ratio of the two nuclei is  $\sim 3.8$ , so the SDSS spectrum is dominated by the brighter one, and the contribution from the fainter one can be neglected. Figure 3(c) shows the color map of  $g-r$  made from SDSS images. The *red-circle* represents the  $3''$  diameter of the fiber aperture, which covers  $\sim 7$  kpc of the galaxy. The  $g-r$  image shows that the central region is bluer than the regions around it. If we attribute the color gradient to the circumnuclear SB, we can estimate the age of the central populations. After converting the  $g-r$  color to  $B-V$  color (Jester et al. 2005), we find that the stellar populations at the center may be less than 100 Myr (BC03; assuming  $Z_\odot$ ).

Figure 3 has clearly indicated that this galaxy is undergoing a later merger phase. Furthermore, the  $H$ -band absolute magnitude is acquired from the 2MASS All-Sky Extended Source Catalog through the GATOR<sup>4</sup> catalog query service. The standard isophotal photometry magnitude is

<sup>4</sup> GATOR web site (<http://irsa.ipac.caltech.edu/applications/Gator>).

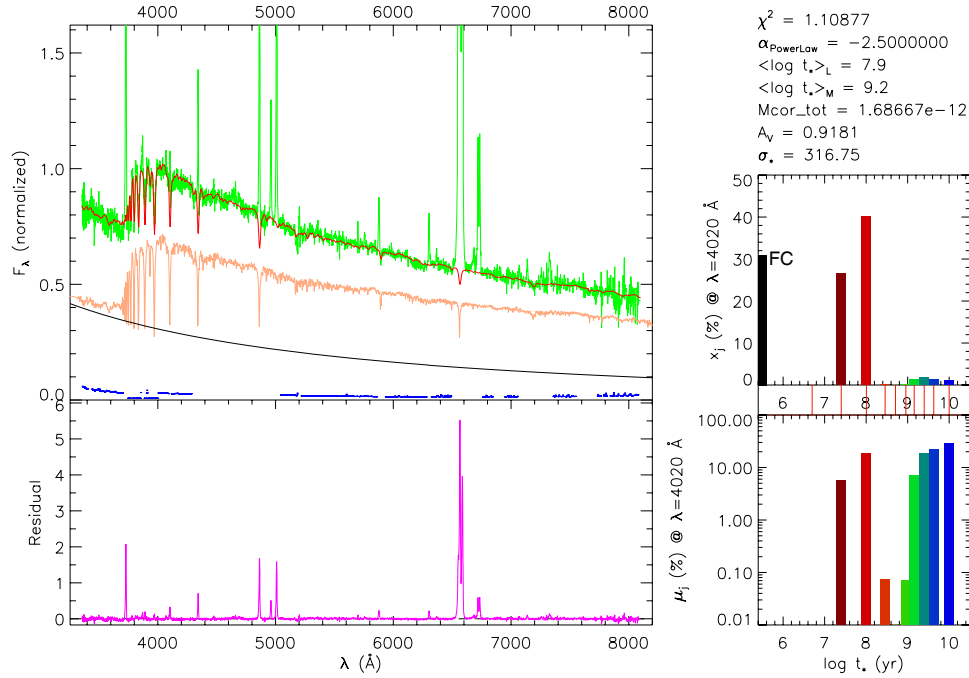


**Fig. 2** Spectral synthesis of IRAS F21013–0739. *Top-left*: the observed spectrum  $O_\lambda$  (green), the model synthetic spectrum  $M_\lambda$  (red), the synthetic stellar component spectrum (beige), the power-law spectrum (black), and the error spectrum (blue) with the gaps meaning the masked regions and the thrice weighted absorption lines. *Bottom-left*: the residual spectrum  $E_\lambda$  (purple). *Right*: light (*top*) and mass (*bottom*) weighted stellar population fractions  $x_j$  and  $\mu_j$ , respectively. The inserted panels on the *right* mark the ages of the stellar population templates.  $M_{\text{cor\_tot}}$  is the present stellar mass converted from the model stellar populations. The flux intensities of the two *left* panels are both normalized at  $4020 \text{ \AA}$  by  $6.968 \times 10^{-16} \text{ erg s}^{-1} \text{ cm}^{-2} \text{ \AA}^{-1}$ .

adopted here, which gives  $M_H = -25.1$ . It is  $\sim 2$  times as luminous as  $L^*$  ( $M_H = -24.2$ ; Colina et al. 2001) galaxies, so the galaxy could be a merger system involving massive ( $\geq L^*$ ) galaxies.

The infrared luminosity ( $L_{\text{IR}}(8 - 1000 \mu\text{m})$ ) is calculated from the flux density at  $60 \mu\text{m}$  through

$$L_{\text{IR}}(8 - 1000 \mu\text{m}) \approx 2L_{60 \mu\text{m}} \quad (1)$$

(Lawrence et al. 1989; Bushouse et al. 2002; Arribas et al. 2004; Wang 2008) where  $L_{60 \mu\text{m}}$  is the luminosity at  $60 \mu\text{m}$ . The derived IR luminosity is  $L_{\text{IR}}(8 - 1000 \mu\text{m}) = 10^{11.53} L_\odot$ , so this object is an LIRG.

IR magnitudes of *Spitzer* IRAC and MIPS bands are listed in Table 2. IRAC colors of  $[3.6] - [4.5]$  and  $[5.8] - [8.0]$  are  $[3.6] - [4.5] = 0.45$  and  $[5.8] - [8.0] = 2.77$ , respectively. When using the reference of Stern et al. (2005, fig. 1), this galaxy falls in the region for galaxies, close to the M82 line, and far from broad-line AGNs. The Genzel IR Diagnostic Diagram is adopted to estimate the relative SB/AGN contribution, which can be found in the following section.

The 1.4 GHz luminosity is  $1.86 \times 10^{23} \text{ W Hz}^{-1}$  (Basu-Zych et al. 2007), correlating with the  $60 \mu\text{m}$  luminosity very well like other IR-selected galaxies (Yun et al. 2001), which follow the

**Table 2** Magnitudes from Spitzer IRAC and MIPS Image Aperture Photometry

Band ( $\mu\text{m}$ )	mag (Vega)	Flux (mJy)
3.6	13.17	1.50
4.5	12.72	1.47
5.8	11.93	1.97
8.0	9.16	13.67
24	4.19	151.2
70	0.74	391.3
160	−0.16	183.5

well-known radio-FIR correlation. The “ $q$ ” parameter for determining IR/radio excess is calculated through the formula given by Condon et al. (1991) and it is derived to be  $q = 2.45$ , close to the average value  $q = 2.34$  of the IRAS 2 Jy sample (Yun et al. 2001). This indicates that IRAS F21013–0739 is not a radio-excess object.

## 4.2 Spectroscopic Properties

The residual spectrum  $E_\lambda$  (the purple spectrum of the bottom-left panel) in Figure 2 can be used to measure optical emission lines, since the stellar component and the AGN continuum have been removed. Emission lines are modeled by the SPECFIT task in the IRAF-STSDAS package. We recognize a broad wing in the  $H\alpha$  line, and a blue wing asymmetry in the  $H\beta$  line, which may be broad components coming from the broad-line region (BLR). However, the widths of the two additional components are different. If these lines are powered by an AGN, like Seyfert 1.8 or Seyfert 1.9 galaxies, the broad component of  $H\beta$  could become more extinct than  $H\alpha$ , so its width should certainly be narrower than  $H\alpha$ . We use two Gaussian profiles to fit their narrow and broad components. Line centers are fitted by narrow profiles and their widths are fixed to the same value, but the line wings are given different widths.  $[\text{O III}] \lambda 4959$  or  $[\text{O III}] \lambda 5007$  cannot be fitted by a single Gaussian line, so we use two Gaussian profiles to fit each line, and the summation of the two components’ fluxes is taken as the integrated line fluxes. Line widths are fixed to be the same between line pairs of  $[\text{O III}]_N$ ,  $[\text{O III}]_B$ ,  $[\text{N II}]$  and  $[\text{S II}]$  doublets. The flux ratios of  $[\text{O III}]_N$ ,  $[\text{O III}]_B$  and  $[\text{N II}]$  doublets are fixed at their theoretical values. Fitting results are shown in Figure 4.

The Spitzer IRS low resolution MIR spectrum is shown in Figure 5 as the purple line. The continuum shows a broken power-law at  $\sim 20 \mu\text{m}$ , which may be due to warm dust component emission (Buchanan et al. 2006, and references therein). No clear  $10 \mu\text{m}$  silicate feature in emission or absorption can be recognized. MIR spectra of diverse types of galaxies are also plotted in Figure 5 for comparison. These spectra are all normalized at  $15 \mu\text{m}$ . The red, green, blue and black lines are average spectra of quasars, Seyfert 1s, Seyfert 2s and ULIRGs respectively, which are taken from Hao et al. (2007); the brown line is the average spectrum of IR quasars taken from Cao et al. (2008). The spectrum of IRAS F21013–0739 shows a similar spectral shape as Seyfert galaxies and IR quasars, and falls within the 1 sigma range of the Seyfert 2 sample<sup>5</sup>. MIR emission lines of polycyclic aromatic hydrocarbon (PAH)  $6.2$ ,  $7.7$ ,  $8.6$  and  $11.3 \mu\text{m}$ ,  $[\text{Ne II}] 12.8 \mu\text{m}$ ,  $[\text{O IV}] 25.9 \mu\text{m}$ , etc., are detected. These emission lines are modeled with single Gaussian profiles to measure line fluxes using the software SMART. The derived emission line properties are listed in Table 3. Also listed are optical line properties, which do not have aperture or extinction correction. The uncertainties in Columns (2) and (3) are given by the SPECFIT task and SMART for optical and MIR lines.

The flux ratios of  $[\text{O III}] \lambda 5007/H\beta_N$  and  $[\text{N II}] \lambda 6583/H\alpha_N$  are  $1.424 (< 3)$  and  $0.806 (> 0.6)$ , indicating a position on the BPT (Baldwin, Phillips & Terlevich) diagram where composite objects

<sup>5</sup> The average spectra and the 1 sigma range of each sample can be found at [http://isc.astro.cornell.edu/~hao/AGN/Ave/ave\\_spectra.html](http://isc.astro.cornell.edu/~hao/AGN/Ave/ave_spectra.html)

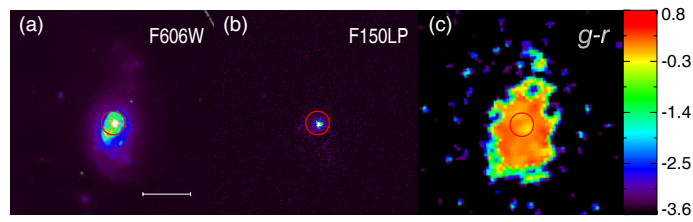


**Fig. 3** *HST* and SDSS images of IRAS F21013–0739. (a) *HST* WFPC2 F606W filter image; (b) *HST* ACS SBC F150LP filter image; (c) SDSS  $g-r$  color map. The *red-circle* represents the 3'' diameter fiber aperture of the SDSS spectrograph. The images are displayed at the same scales, and the scale bar represents 20 kpc.

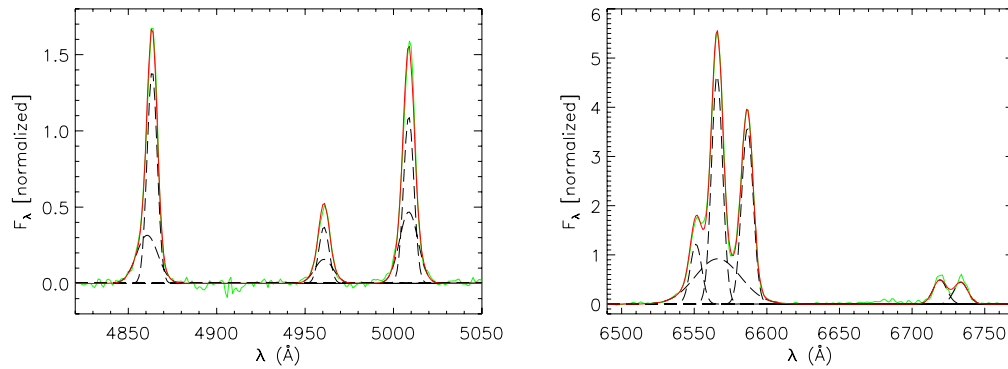


**Fig. 4** Fits to the emission lines. Flux intensities are inherited from the residual spectrum in Fig. 2. The observed line profile (*green-solid*), the model profile (*red-solid*), each line and different components (*black-dashed*) are plotted in each panel. *Left*:  $H\beta+[O\text{ III}]$  region; *right*:  $H\alpha+[N\text{ II}]+[S\text{ II}]$  region.

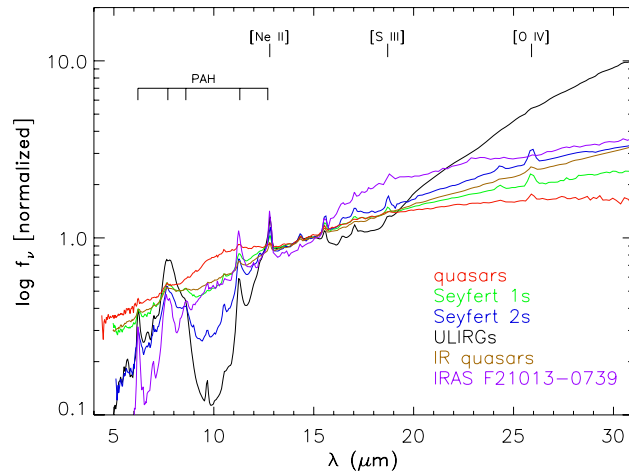


**Fig. 5** MIR average spectra of diverse types of galaxies. Spectra of quasars (*red*), Seyfert 1s (*green*), Seyfert 2s (*blue*) and ULIRGs (*black*) are taken from Hao et al. (2007); the spectrum of IR quasars (*brown*) is taken from Cao et al. (2008); the *purple* line is the spectrum of IRAS F21013–0739.

**Table 3** Emission line Properties of IRAS F21013–0739

Optical Lines (1)	Flux <sup>1</sup> (2)	FWHM (km s <sup>-1</sup> ) (3)
[O II]λ3727	15.00±0.77	535.95±22.08
[O I]λ6300	2.20±0.14	450.27±26.45
Hβ <sub>N</sub>	9.89±0.71	410.83±11.38
Hβ <sub>B</sub>	4.78±0.66	878.42±50.16
Hα <sub>N</sub>	44.51±1.86	410.83±11.38
Hα <sub>B</sub>	36.05±2.15	1681.6±87.92
[O III]λ4959 <sub>N</sub>	2.66±0.61	409.06±38.50
[O III]λ4959 <sub>B</sub>	2.04±0.61	733.31±58.98
[O III]λ5007 <sub>N</sub>	7.97±1.83	409.06±38.50
[O III]λ5007 <sub>B</sub>	6.11±1.83	733.31±58.98
[N II]λ6548	12.12±0.38	429.30±10.22
[N II]λ6583	35.88±1.12	429.30±10.22
[S II]λ6716	5.97±0.33	427.80±16.06
[S II]λ6731	5.52±0.32	427.80±16.06
MIR Lines	Flux <sup>2</sup>	
PAH 7.7 μm	2.65±0.21	
[Ne II] 12.8 μm	1.14±0.13	
[O IV] 25.9 μm	0.13±0.009	

<sup>1</sup> Optical line fluxes are measured within the 3'' fiber aperture, without extinction correction, and in units of  $6.967944 \times 10^{-16}$  erg s<sup>-1</sup> cm<sup>-2</sup>;

<sup>2</sup> MIR line fluxes are in units of  $10^{-13}$  erg s<sup>-1</sup> cm<sup>-2</sup>.

are located. Composite objects are traditionally classified into type 2 AGNs (Heckman 1980), and the AGN spectra may have been diluted or contaminated by neighboring H II regions (Ho et al. 1993). The Hα line has a broad component with FWHM = 1681.6 km s<sup>-1</sup>, and the FWHMs of [O III] doublets are > 400 km s<sup>-1</sup>, both of which indicate the existence of an AGN (Hao 2004). Furthermore, its position on the ISO SWS diagnostic diagram (Genzel et al. 1998) is also obtained. The [O IV]/[Ne II] flux ratio is 0.11, and the PAH 7.7 μm line strength is 0.93. Such ratios position this galaxy in the 50% AGN region of the SWS diagnostic diagram. The IR diagnostic result suggests that the IR emission is possibly dominated by the host galaxy, and it might harbor an AGN but not a broad-line AGN.

### 4.3 Optical Aperture and Extinction Correction

Figure 3 has shown that the 3'' fiber does not cover the whole galaxy, and the difference between *fiberMags* and *petroMags* in Table 2 can be about 1 magnitude in some bands, so aperture corrections are necessary. The correction method we use here is the one only for the SB component, as in M10 where

$$A = \frac{L_{\star\text{Petro}}}{L_{\star\text{fiber}}} = \frac{10^{-0.4(m_{\text{Petro}} - m_{\text{AGN}})} - 1}{10^{-0.4(m_{\text{fiber}} - m_{\text{AGN}})} - 1}. \quad (2)$$

The variables' meanings and the ranges of application are the same as M10.

Emission-line fluxes have to be corrected for dust extinction, and the correction factors vary with wavelengths. We use the extinction curve given by Calzetti et al. (2000) (Cal00) and Leitherer et al. (2002) (Lei02), as in M10. The color excess for nebular gas emission lines is denoted by  $E_g(B-V)$  and is directly estimated through Balmer decrement, the line ratio  $H\alpha_N/H\beta_N = 4.5$ , whose intrinsic flux ratio is  $(H\alpha_N/H\beta_N)_0 = 2.87$  assuming temperature  $T = 10000$  K and case B recombination (Osterbrock 1989).  $E_g(B-V)$  is derived to be  $E_g(B-V) = 0.42$ . For comparison, the spectral synthesis gives  $A_V = 0.9181$ , which can be translated to  $E_g(B-V) = 0.52$  through the Calzetti curve.

It does not differ very much from the Balmer decrement estimated one, so the spectral synthesis and emission line fittings are reasonable.

#### 4.4 SFR and Black-Hole Mass

Star-forming activity is demonstrated by the presence of [O II] emission, PAH emission and recent starburst history. A simple estimation of star formation rate (SFR) can be calculated through

$$\text{SFR}([\text{O II}])(M_{\odot} \text{ yr}^{-1}) = (6.58 \pm 1.65) \times 10^{-42} L_{[\text{O II}]}(\text{erg s}^{-1}) \quad (3)$$

(Kewley et al. 2004), where  $L_{[\text{O II}]}$  is the extinction corrected luminosity of [O II]  $\lambda 3727$ , which gives an SFR of  $55.1 M_{\odot} \text{ yr}^{-1}$ . The aperture corrected (a factor of  $\sim 4.5$ , adopting Eq. (2)) [O II] luminosity gives an SFR of  $250.4 M_{\odot} \text{ yr}^{-1}$ , which is too high for LIRGs. Since we have found that the SB activity takes place mainly in the central region of the galaxy (see Sect.3), where the fiber aperture covers, the SFR with aperture correction should just be taken as an upper-limit. Abundance correction for the [O II] SFR calculation has also been considered. The metallicity  $\log(\text{O}/\text{H}) + 12$  is estimated through the  $R_{23}$  ratio,  $([\text{O II}]\lambda 3727 + [\text{O III}]\lambda 4959, 5007)/\text{H}\beta$ , whose fluxes are extinction corrected. The  $\log(\text{O}/\text{H}) + 12$  is about 8.89, so the abundance correction can be taken using Kewley et al.'s (2004) calibration, equation (9) in their paper. The abundance corrected SFR is  $56.7 M_{\odot} \text{ yr}^{-1}$ . Spitzer photometry provides us another way to estimate the SFR.

Wu et al. (2005) and Zhu et al. (2008) both have given the correlation between the IRAC  $8 \mu\text{m}$  broadband flux and the SFR from the  $\text{H}\alpha$  calibration. From the IRS spectrum of IRAS F21013–0739, we found that the  $8 \mu\text{m}$  band flux is dominated by PAH emission, which is a nice SFR indicator. The old obscured stellar population of this source is very weak, so we directly calculate the SFR through the aperture corrected  $8 \mu\text{m}$  band flux and obtain  $\sim 39 M_{\odot} \text{ yr}^{-1}$ , which supports the one obtained from the [O II] luminosity inside the SDSS aperture.

For SB galaxies, SFR can also be estimated through IR luminosity (Kennicutt 1998, and references therein). As for IRAS F21013–0739, since it contains both SB and AGN components, the total IR luminosity  $10^{11.53} L_{\odot}$  only suggests an upper limit of SFR, which is  $58.2 M_{\odot} \text{ yr}^{-1}$ . The spectral synthesis has given the SB fraction of the galaxy, so the SFR can only be estimated by the IR luminosity from the SB rate. Such calculation will be given in the following section.

The BH mass can be estimated through the formula given by Greene & Ho (2005)

$$M_{\text{BH}} = (2.0_{-0.3}^{+0.4}) \times 10^6 \left( \frac{L_{\text{H}\alpha_{\text{B}}}}{10^{42} \text{ erg s}^{-1}} \right)^{0.55 \pm 0.02} \times \left( \frac{\text{FWHM}_{\text{H}\alpha}}{10^3 \text{ km s}^{-1}} \right)^{2.06 \pm 0.06} M_{\odot}, \quad (4)$$

where  $L_{\text{H}\alpha_{\text{B}}}$  is the  $\text{H}\alpha_{\text{B}}$  luminosity corrected by dust extinction that is inferred from the Balmer decrement and by adopting the Calzetti extinction curve. Since the SDSS fiber aperture covers  $\sim 7$  kpc, when definitely including the broad-line region, we do not carry out aperture correction on  $L_{\text{H}\alpha_{\text{B}}}$ . The derived BH mass is  $M_{\text{BH}} = 1.6 \times 10^7 M_{\odot}$ . Noting that the broad components of the  $\text{H}\beta$  line are much more likely to be extinct and cannot be recovered by extinction correction, the  $\text{H}\alpha$  line may also not be recoverable by extinction correction, so the above BH mass may be underestimated and can be regarded as a lower-limit.

The Eddington ratio  $L_{\text{bol}}/L_{\text{Edd}}$  is calculated adopting the bolometric luminosity  $L_{\text{bol}} \approx 9\lambda L_{\lambda}(5100 \text{ \AA})$  (Kaspi et al. 2000), where  $L_{\lambda}(5100 \text{ \AA})$  is the AGN optical continuum luminosity at  $5100 \text{ \AA}$ . The inferred Eddington ratio is  $L_{\text{bol}}/L_{\text{Edd}} = 0.15$ , which is typical of Palomar-Green (PG) quasars (median=0.24; Hao et al. 2005).

#### 4.5 FIR Luminosity in the Past

We have developed a method to trace IR luminosity back to the past at a given epoch in M10. The outline of the method is that (1) we reconstruct the UV-to-optical spectrum making use of the stellar

component mass and the dust extinction  $A_V$  that is obtained from the spectral synthesis, through the formula

$$\begin{aligned}
 F_e(\lambda, t) &= F_i(\lambda, t) \times 10^{-0.4(A_\lambda - A_V)} \\
 &= \left[ M_{\text{abs}} \sum_{j=1}^N \frac{\mu_j}{f_{\star, j, t_0}} f_{\star, j, t} B_{\lambda, j, t} + F_p(\lambda) \right] \times 10^{-0.4 \left[ E_s(B-V) k'(\lambda) - E_s(B-V) k'_V \right]} \quad (5)
 \end{aligned}$$

where  $F_e(\lambda, t)$  is the observed spectrum (extinct by dust) at a given time  $t$ ;  $t$  can be the time in the past or at the present (equal to  $t_0$ ),  $F_i(\lambda, t)$  is the intrinsic emission without dust extinction at time  $t$ ,  $M_{\text{abs}}$  is the present absolute stellar mass calculated from `Mcor_tot` obtained from the spectral synthesis and is derived to be  $2.2 \times 10^{10} M_\odot$  after aperture correction through Equation (2),  $f_{\star, j, t}$  is the fraction of the remaining stellar mass compared to the initial mass of the population  $j$  at time  $t$ ,  $f_{\star, j, t_0}$  is such a fraction at present,  $f_{\star, j, t}$  and  $f_{\star, j, t_0}$  are in the range  $0 < f_{\star, j, t_0}, f_{\star, j, t} \leq 1$ ,  $B_{\lambda, j, t}$  are BC03 SSP templates without normalization, and  $F_p(\lambda)$  is a double power-law spectrum of AGN (if needed). The spectral indices of the power-law we use here are given by Hatziminaoglou et al. (2008) where  $\alpha = -1$  for  $\lambda < 1250 \text{ \AA}$  and  $\alpha = -2$  for  $\lambda \geq 1250 \text{ \AA}$ .  $E_s(B-V)$  is the color excess for the stellar and AGN continuum spectrum and  $E_s(B-V) = 0.44 E_g(B-V)$  (Cal00). Also,  $k'(\lambda)$  is the extinction curve of Cal00 and Lei02; (2) we calculate the UV-to-optical flux absorbed by dust and re-emitted to IR through

$$L_{\text{IR}, t} = \int_{912}^{9000} [F_i(\lambda, t) - F_e(\lambda, t)] d\lambda. \quad (6)$$

The present IR luminosity calculated in this way is  $L_{\text{IR}, 0} = 10^{11.61} L_\odot$ , which is close to the observed  $L_{\text{IR}} = 10^{11.53} L_\odot$ . The contributions from SB and AGN components are calculated separately to be  $L_{\text{star}, \text{IR}} = 10^{11.43} L_\odot$  and  $L_{\text{AGN}, \text{IR}} = 10^{11.13} L_\odot$ , respectively. The SB contributes  $\sim 67\%$  of the FIR luminosity, two thirds of the total FIR budget. For comparison, we fit the IR spectral energy distribution (SED) from Spitzer spectra and photometry data points with SB and AGN SED templates to estimate their IR contributions more directly. The SB template is from Siebenmorgen & Krügel (2007), and the AGN template is from Siebenmorgen et al. (2004). The fitting result is shown in Fig. 6. The SB template contributes  $\sim 70\%$  of the integrated IR energy. It is close to the estimation from optical spectrum reconstruction, which also suggests that the SB dominates the IR emission.

The current SFR can be estimated again using the relation between  $L_{\text{FIR}}(8 - 1000 \mu\text{m})$  and SFR (Kennicutt 1998). Since the host galaxy contributes  $\sim 67\%$  of the FIR luminosity, we obtain  $\text{SFR} = 46.9 M_\odot \text{ yr}^{-1}$ .

The past IR luminosity calculation is carried out just considering the stellar component, since the AGN activity in the past is hard to estimate. The dust extinction is assumed to be at the same level as present. At 25, 100, 290 and 500 Myr ago, the estimated IR luminosities from the host galaxy were  $L_{\text{IR}, 25\text{M}} = 10^{12.0} L_\odot$ ,  $L_{\text{IR}, 100\text{M}} = 10^{12.5} L_\odot$ ,  $L_{\text{IR}, 290\text{M}} = 10^{10.3} L_\odot$  and  $L_{\text{IR}, 500\text{M}} = 10^{9.7} L_\odot$ . Therefore, during the most active star-forming epoch, the galaxy was undergoing a ULIRG phase, and the ULIRG phase lasted for  $\sim 100$  Myr. If we consider the AGN's contribution in the past, the IR luminosity should be higher.

## 5 DISCUSSION AND CONCLUSION

The optical emission line widths have shown that IRAS F21013–0739 is neither a type I AGN nor a classical quasar, but many evidences support the existence of an AGN (see Sects. 3 and 4). When plotting it on the diagram of the IR spectral index  $\alpha(60, 25)$  (defined as  $\alpha(\lambda_1, \lambda_2) = -\frac{\log[F(\lambda_2)/F(\lambda_1)]}{\log(\lambda_2/\lambda_1)}$ ) versus the IR/optical excess  $L_{\text{IR}}/L_{5000}$  (Fig. 7), it falls on a transitional position between IR quasars and PG quasars. Since the temperature of dust heated by stars is lower than that by an AGN, we can expect that as the SFR decreases, IRAS F21013–0739 could move to join the quasar region in

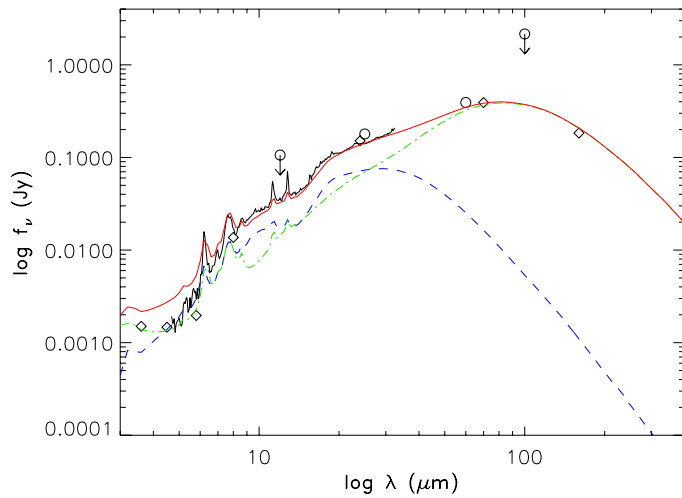


**Fig. 6** IR SED fitting with SB and AGN SED templates. *Black-solid-line*: The IRS spectrum from Spitzer; *black-diamond*: IRAC and MIPS photometry points; *black-circle*: IRAS photometric points and upper-limits; *green-dot-dashed-line*: SB model SED from Siebenmorgen & Krügel (2007); *blue-dashed-line*: AGN model SED from Siebenmorgen et al. (2004); *red-line*: the summation of SB and AGN SEDs.

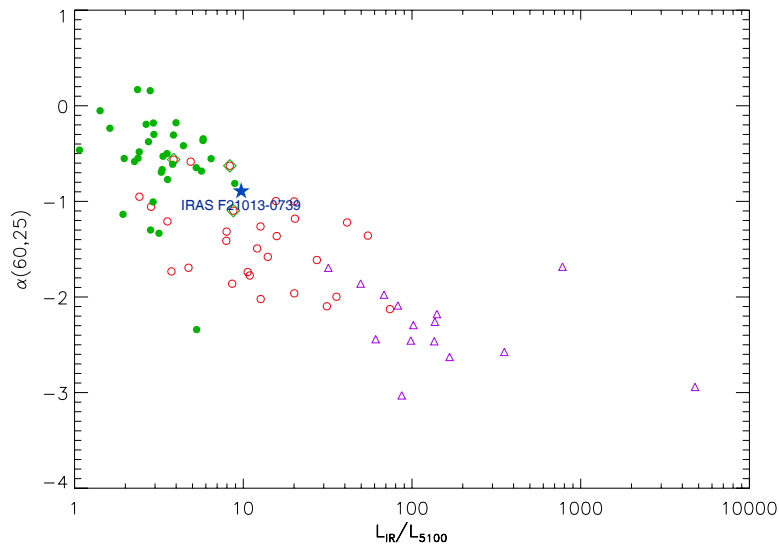


**Fig. 7** IR spectral index  $\alpha(60, 25)$  vs. the IR excess,  $L_{\text{IR}}/L_{5100}$ . The *red* open circles represent IR quasars from Hao et al. (2005); the *green* filled circles represent PG quasars from Hao et al. (2005); the *purple* open triangles represent 15 ULIRGs, which are selected from Kim & Sanders (1998b) and have SDSS spectra; the three *red* open circles enclosed by *green* diamonds represent IR quasars which are also PG quasars.

the diagram. Observational evidences are accumulating that AGN feedbacks in starburst galaxies are powerful forces for expelling cool gas and shutting down star formation (Tremonti et al. 2007; Cao et al. 2008). As a composite type galaxy and one with obscured BLR, it may be the same as the case Koulouridis et al. (2006) proposed, where the AGN emission may become greatly extinct by a torus or the star-forming host galaxy, and its emission may be contaminated by the surrounding star-formation, so it is a potential classical AGN when the dust content has dissipated and the star-formation fades. The galaxy's merger phase could have a timescale of a few  $\times 10^8$  yr (Binney & Tremaine 1987), and the spectral synthesis shows SB activity has occurred since 100 Myr; similar timescales imply that the SB activity was triggered by galaxy mergers. Recalling that the IR luminosities in the past epochs have indicated the galaxy was probably a ULIRG  $\sim 100$  Myr ago, we conclude that we are possibly witnessing a ULIRG that was generated from massive galaxy ( $\geq L_*$ ) mergers evolving into a type 2 LIRG, and which will possibly evolve into an AGN.

**Acknowledgements** The authors are grateful to Dr. Cai-Na Hao for her data through private communication. This project is supported by the National Natural Science Foundation of China (Grant Nos. 10833006, 10773014, and 10978014) and the Ministry of Science and Technology National Basic Science program (973 Program, Grant No. 2007CB815406).

This work is based on the data from FIRST, IRAS and SDSS observations. Funding for the SDSS and SDSS-II has been provided by the Alfred P. Sloan Foundation, the Participating Institutions, the National Science Foundation, the U.S. Department of Energy, the National Aeronautics and Space Administration, the Japanese Monbukagakusho, the Max Planck Society, and the Higher Education Funding Council for England. The SDSS Web Site is <http://www.sdss.org/>. This work makes use of data products from the 2MASS, which is a joint project of the University of Massachusetts and the Infrared Processing and Analysis Center/California Institute of Technology, funded by the National Aeronautics and Space Administration and the National Science Foundation. This work is also based on observations made with the Spitzer Space Telescope, which is operated by the Jet Propulsion Laboratory, California Institute of Technology under a contract with NASA. The IRS was a collaborative venture between Cornell University and Ball Aerospace Corporation funded by NASA through the Jet Propulsion Laboratory and Ames Research Center. SMART was developed by the IRS Team at Cornell University.

## References

- Antonucci, R. 1993, *ARA&A*, 31, 473  
 Arribas, S., & Colina, L. 2003, *ApJ*, 591, 791  
 Arribas, S., Bushouse, H., Lucas, R. A., Colina, L., & Borne, K. D. 2004, *AJ*, 127, 2522  
 Basu-Zych, A. R., Schiminovich, D., Johnson, B., et al. 2007, *ApJS*, 173, 457  
 Binney, J., & Tremaine, S. 1987, *Galactic Dynamics* (Princeton: Princeton Univ. Press)  
 Blanton, M. R., et al. 2003, *AJ*, 125, 2348  
 Boller, T., Gallo, L. C., Lutz, D., & Sturm, E. 2002, *MNRAS*, 336, 1143  
 Bruzual G., & Charlot, S., 2003, *MNRAS*, 344, 1000 (BC03)  
 Buchanan, C. L., Gallimore, J. F., O'Dea, C. P., Baum, S. A., Axon, D. J., Robinson, A., Elitzur, M., & Elvis, M. 2006, *AJ*, 132, 401  
 Bushouse H. A., Borne K. D., Colina L. et al. 2002, *ApJS*, 138, 1  
 Calzetti, D., Armus, L., Bohlin, R. C. et al., 2000. *ApJ*, 533, 682 (Cal00)  
 Canalizo, G., & Stockton, A. 2000, *AJ*, 120, 1750  
 Canalizo, G., & Stockton, A. 2001, *ApJ*, 555, 719  
 Cao, C., Wu, H., Wang, J. L., Hao, C. N., Deng, Z. G., Xia, X. Y., & Zou, Z. L. 2006, *ChJAA* (*Chin. J. Astron. Astrophys.*), 6, 197  
 Cao, C., Xia, X. Y., Wu, H., Mao, S., Hao, C. N., & Deng, Z. G. 2008 *MNRAS*, 390, 336

- Cid Fernandes, R., Gu, Q., Melnick, J., Terlevich, E., Terlevich, R., Kunth, D., Rodrigues Lacerda, R., & Joguet, B. 2004, MNRAS, 355, 273
- Cid Fernandes R., Mateus A., Sodré L., Stasińska G., Gomes J. M. 2005, MNRAS, 358, 363
- Clements, D. L., Sutherland, W. J., McMahon, R. G., & Saunders, W. 1996, MNRAS, 279, 477
- Colina, L., et al. 2001, ApJ, 563, 546
- Condon, J. J., Anderson, M. L., & Helou, G. 1991, ApJ, 376, 95
- Dasyra, K. M., et al. 2006, ApJ, 651, 835
- Franceschini, A., et al. 2003, MNRAS, 343, 1181
- Francis, P. J. 1996, Publ. Astron. Soc. Australia, 13, 212
- Genzel, R., Lutz, D., Sturm, E., et al. 1998, ApJ, 498, 579
- Genzel, R., Tacconi, L. J., Rigopoulou, D., Lutz, D., & Tecza, M. 2001, ApJ, 563, 527
- Greene, J. E., & Ho, L. C., 2005, ApJ, 630, 122
- Gu, Q. S., Huang, J. H., Su, H. J., & Shang, Z. H. 1997, A&A, 319, 92
- Hao, C. N., Xia, X. Y., Mao, S., Wu, H., & Deng, Z. G. 2005, ApJ, 625, 78
- Hao, L. 2004, Ph.D. thesis, Princeton Univ.
- Hao, L., Weedman, D. W., Spoon, H. W. W., et al. 2007, ApJ, 655, L77
- Hatziminaoglou, E. et al. 2008, MNRAS, 386, 1252
- Heckman T. M., 1980, A&A, 87, 152
- Higdon, S. J. U., et al. 2004, PASP, 116, 975
- Ho L. C., Filippenko A. V., Sargent W. L. W., 1993, ApJ, 417, 63
- Hopkins, A. M., et al. 2003, ApJ, 599, 971
- Hou, L. G., Wu, X. B., & Han, J. L. 2009, ApJ, 704, 789
- Houck, J. R., et al. 1984, ApJ, 278, L63
- Houck, J. R., et al. 2004, ApJS, 154, 18
- Jester, S., et al. 2005, AJ, 130, 873
- Kaspi, S., Smith, P. S., Netzer, H., Maoz, D., Jannuzi, B. T., & Giveon, U. 2000, ApJ, 533, 631
- Kawakatu, N., Anabuki, N., Nagao, T., Umemura, M., & Nakagawa, T. 2006, ApJ, 637, 104
- Kennicutt, R. C., Jr. 1998, ARA&A, 36, 189
- Kewley, L. J., Geller, M. J., & Jansen, R. A. 2004, AJ, 127, 2002
- Kewley, L. J., Heisler, C. A., Dopita, M. A., Lumsden, S. 2001, ApJS, 132, 37
- Kim, D.-C., & Sanders, D. B. 1998, ApJS, 119, 41
- Kim, D.-C., Veilleux, S., & Sanders, D. B. 1998, ApJ, 508, 627
- Kim, D. C., Veilleux, S., & Sanders, D. B. 2002, ApJS, 143, 277
- Koulouridis, E., Chavushyan, V., Plionis, M., Krongold, Y., & Dultzin-Hacyan, D. 2006, ApJ, 651, 93
- Larson, R. B., & Tinsley, B. M. 1978, ApJ, 219, 46
- Lawrence, A., Rowan-Robinson, M., Leech, K. J., Jones, D. H. P., & Wall, J. V. 1989, MNRAS, 240, 329
- Lebouteiller, V., Bernard-Salas, J., Sloan, G. C., & Barry, D. J. 2010, PASP, 122, 231
- Leitherer, C., Li, I.-H., Calzetti, D., & Heckman, T. M. 2002, ApJS, 140, 303 (Lei02)
- Letawe, G., Magain, P., Courbin, F., Jablonka, P., Jahnke, K., Meylan, G., & Wisotzki, L. 2007, MNRAS, 378, 83
- Lutz, D., Veilleux, S., & Genzel, R. 1999, ApJ, 517, L13
- McLeod, K. K., & Rieke, G. H. 1994, ApJ, 431, 137
- Melnick, J., & Mirabel, I. F. 1990, A&A, 231, L19
- Meng, X., Wu, H., Gu, Q., Wang, J., & Cao, C. 2010, ApJ, 718, 928 (M10)
- Murphy, T. W., Jr., et al. 1996, AJ, 111, 1025
- Nandra, K., & Iwasawa, K., 2007, MNRAS, 382, L1
- Nardini, E., et al. 2008, MNRAS, 385, L130
- Nardini, E., Risaliti, G., Watabe, Y., Salvati, M., & Sani, E. 2010, MNRAS, 405, 2505

- Osterbrock, D. E. 1989, *Astrophysics of Gaseous Nebulae and Active Galactic Nuclei* (Mill Valley: University Science Books)
- Pellerin, A., & Robert, C. 2007, *MNRAS*, 381, 228
- Sanders, D. B., Soifer, B. T., Elias, J. H., Madore, B. F., Matthews, K., Neugebauer, G., & Scoville, N. Z. 1988a, *ApJ*, 325, 74
- Sanders, D. B., Soifer, B. T., Elias, J. H., Neugebauer, G., & Matthews, K. 1988b, *ApJ*, 328, L35
- Schlegel, D. J., Finkbeiner, D. P., & Davis, M. 1998, *ApJ*, 500, 525
- Schneider, D. P. et al. 2007, *AJ*, 134, 102
- Schneider, D. P. et al. 2010, *AJ*, 139, 2360
- Siebenmorgen, R., Freudling, W., Krügel, E., & Haas, M. 2004, *A&A*, 421, 129
- Siebenmorgen, R., & Krügel, E. 2007, *A&A*, 461, 445
- Soifer, B. T., et al. 1984, *ApJ*, 278, L71
- Stern, D., Eisenhardt, P., Gorjian, V., et al. 2005, *ApJ*, 631, 163
- Tacconi, L. J., Genzel, R., Lutz, D., Rigopoulou, D., Baker, A. J., Iserlohe, C., & Tecza, M. 2002, *ApJ*, 580, 73
- Tadhunter, C. N., Robinson, T. G., González Delgado, R. M., Wills, K., Morganti, R. 2005, *MNRAS*, 356, 480
- Toomre, A., & Toomre, J. 1972, *ApJ*, 178, 623
- Tremonti, C. A., Moustakas, J., & Diamond-Stanic, A. M. 2007, *ApJ*, 663, L77
- Urry, C. M., & Padovani, P. 1995, *PASP*, 107, 803
- Vanden Berk, D. E. et al. 2001, *AJ*, 122, 549
- Veilleux, S., Kim, D.-C., Sanders, D. B. 1999, *ApJ*, 522, 113
- Veilleux, S., Kim, D.-C., & Sanders, D. B. 2002, *ApJS*, 143, 315
- Veilleux, S., et al. 2009, *ApJS*, 182, 628
- Wang, J. L. 2008, *ChJAA (Chin. J. Astron. Astrophys.)*, 8, 643
- Wolf, M. J., & Sheinis, A. I. 2008, *AJ*, 136, 1587
- Wu, H., Cao, C., Hao, C. N., Liu, F. S., Wang, J. L., Xia, X. Y., Deng, Z. G., & Young, C. K. S. 2005, *ApJ*, 632, L79
- Wu, H., Zou, Z. L., Xia, X. Y., Deng, Z. G. 1998, *A&AS*, 132, 181
- Yuan, T.-T., Kewley, L. J., & Sanders, D. B. 2010, *ApJ*, 709, 884
- Yun, M. S., Reddy, N. A., & Condon, J. J. 2001, *ApJ*, 554, 803
- Zheng, X. Z., Xia, X. Y., Mao, S., Wu, H., & Deng, Z. G. 2002, *AJ*, 124, 18
- Zhu, Y. N., Wu, H., Cao, C., & Li, H. N. 2008, *ApJ*, 686, 155
- Zou, Z., Xia, X., Deng, Z., & Su, H. 1991, *MNRAS*, 252, 593